Research Article | Vol. 29, No. 7 / 29 March 2021 / Optics Express 9960
Optics EXPRESS

Angular velocimetry for fluid flows: an optical sensor using structured light and machine learning

E. F. Strong,[1,6] A. Q. Anderson,[2] M. P. Brenner,[3,4] B. M. Heffernan,[5] N. Hoghooghi,[1] J. T. Gopinath,[2,5] and G. B. Rieker[1,7]

[1]Department of Mechanical Engineering, University of Colorado, Boulder, Boulder, CO 80309, USA
[2]Department of Electrical, Computer, and Energy Engineering, University of Colorado, Boulder, Boulder, CO 80309, USA
[3]John A. Paulson School of Engineering and Applied Sciences, Harvard University, Cambridge, MA 02138, USA
[4]Google Research, 1600 Amphitheatre Parkway, Mountain View, CA 94043, USA
[5]Department of Physics, University of Colorado, Boulder, Boulder, CO 80309, USA
[6]elizabeth.strong@colorado.edu
[7]Greg.Rieker@colorado.edu

Abstract: Most velocimetry approaches for fluid flows measure linear components of the velocity vector; yet, the angular velocity components, particularly at small scales in turbulent flows, also need to be resolved to study energy transfer and other important flow characteristics. Here, we detail an optical sensor approach to determine a component of the angular velocity vector. This approach uses beams of structured light and a machine learning-based analysis. We discuss the methodology to train the machine learning model and test it in experimentally validated simulations. This approach represents an interesting new direction for fluid flow velocimetry which may be extended to sense other flow parameters by selecting different light structures.

1. Introduction

Experimental techniques are critical for studying fluid flows, especially if the flows cannot be studied numerically due to physical restrictions or computational limitations. As such, velocity sensors are a primary class of diagnostic tool. Velocity sensors typically measure linear components of the velocity vector. Yet, many flows have important angular velocity components. In turbulent flows, for example, regions with elevated local angular velocities give rise to and mediate the most salient characteristics of the flow, including how and where energy is dissipated.

Traditionally, the mismatch between that which can be sensed (linear velocities) and that which is of interest (angular velocities) has been addressed by deriving the latter from the former. For example, metrics such as vorticity and circulation which characterize the local rotation of flows are calculated by numerically differentiating measured multi-component linear velocity fields. However, such strategies come at the cost of resolution, as the numerical differentiation inherently introduces spatial uncertainty. While increasing the density of the field samples can increase the spatial resolution, increasing the number of samples comes the cost of reduced temporal resolution. Thus, if a high degree of temporal resolution is required, poor spatial resolution may result. To refine the spatial and temporal resolutions of measurements which quantify rotation, we seek to measure a component of the angular velocity field without needing to first measure components of the linear velocity fields. This direct strategy will facilitate measurements with

#417210 https://doi.org/10.1364/OE.417210
Journal © 2021 Received 16 Dec 2020; revised 22 Feb 2021; accepted 23 Feb 2021; published 16 Mar 2021

Optics EXPRESS

both short temporal and small spatial resolutions, positioning the measurements well for studying flows which change rapidly in both time and space.

Our sensor uses a strategy common in fluid velocity sensing: seeding the flow with small particles which scatter light. Assuming the particles are sized properly so they travel faithfully with the flow [1], their velocities are assumed to match the velocity of the flow around them. When these particles pass through an optical probe beam, the light they scatter is imaged or collected on a photodetector. Information regarding the size, surface properties, and kinematics of the reflector as well as characteristics of the probe beam such as its intensity are encoded in the scattered signal and can be extracted using appropriate signal processing techniques. Examples of existing techniques which calculate linear components of flow velocities from the light scattered by seeded particles include field sensors like particle image velocimetry (PIV) and point sensors like laser Doppler velocimetry (LDV). Other techniques, such as spatial filtering velocimetry, imprint temporal periodicity into the scattered light signal using spatially periodic masks [2], gratings [3], or optical fiber arrays [4]. These and related flow visualization techniques have been developed extensively, and are commonly used in research and development settings in contexts ranging from flume experiments to study coral reefs [5,6] to blood flow [7] to combustion systems [8,9].

In this paper, we build on these earlier approaches that probe the fluid with structured light (light with engineered phase, polarization, and intensity profiles). In particular, we take advantage of structured light that is tailored to match particular properties we wish to measure (e.g. a pattern with radial symmetry to measure to measure angular velocity [10]), while allowing for resulting scattered light signals to be complicated with no simple relationship to the flow property (e.g. wavelength shift to velocity in LDV). In order to ascertain a correlation between these expected signals and the angular velocity, we train a modern machine learning regression model to interpret the signals. We demonstrate this approach by measuring angular velocity using the interference of two conjugate beams with orbital angular momentum (OAM). To the best of our knowledge, this is the first time that structured light and machine learning have been used together in a velocimetry application.

Our angular velocity sensor is closely related to LDV. The behavior of both our sensor and LDV can be described in the spatial domain. Interference fringes (intensity modulations) generated by superimposing two coherent beams of light comprise the probe beam. Particles traveling through these fringes scatter light proportionally to the local intensity. In one configuration of LDV [11], interfering plane waves give rise to sinusoidal fringes. As depicted in Fig. 1(a) and Fig. 1(b), the distance between fringes multiplied by the frequency at which the scattered light is modulated yields the component of the velocity orthogonal to the fringes.

Modifications to the structure of the probe beam can yield alternative interference patterns which can be used to sense different properties of the flow. For example, the fan-like fringes created by interfering light with cylindrical wavefronts can be used to infer velocity gradients close to a wall [12–14]. Likewise, radial interference fringes can be used to measure angular velocities [10,15–17]. As shown in Fig. 1(c) and Fig. 1(d), the angular velocity of a particle traveling on a circular trajectory concentric with radial interference fringes can be determined from the product of the radial fringe spacing and the intensity modulation frequency, $\Omega = \Delta\phi \times f_{mod}$ [15,17]. In most fluid flows, however, particle orbits are not concentric with the probe beams, and orbit radii may be larger than the size of the beam. What results is a signal processing challenge: no one-to-one relationship between the angular velocity and the expected signal necessarily exists (compare the signals in Fig. 1(d) and Fig. 1(f) which correspond to the same angular velocity). These more complex scenarios therefore require an alternative strategy for signal analysis. The sensor concept that we develop in this paper accommodates complicated signals with a machine learning-based signal processing scheme.

Optics EXPRESS

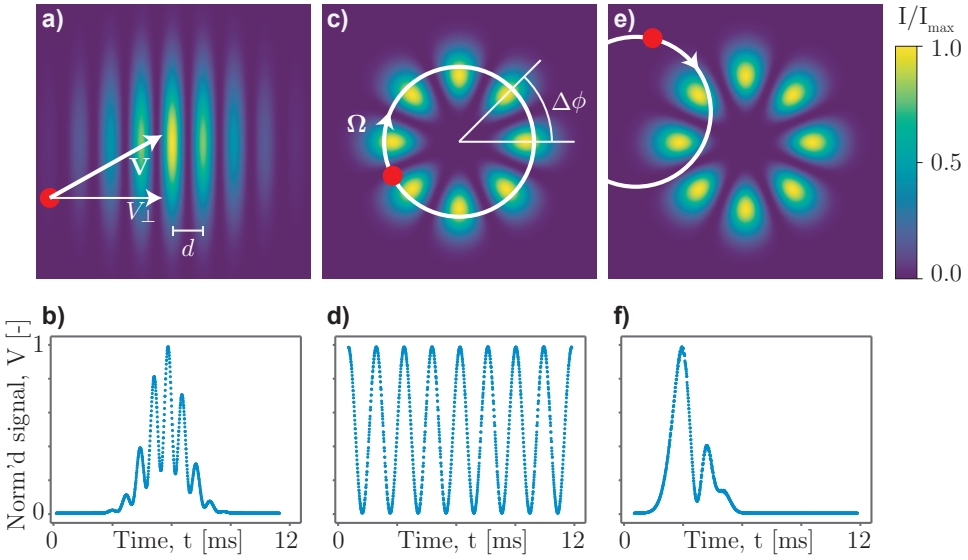

Fig. 1. The light scattered by a particle traveling through interference fringes is encoded with information regarding the particle's kinematics. a, c, f) Simulated schematics of scattering particles (red dots, radii r) traveling on trajectories (indicated with the bold white line) which pass through spatially varying intensity fields created by a) interfering two plane waves with a relative angle of 5.73° or c, f) interfering conjugate Laguerre Gauss beams with $l = \pm 4$ and $p = 0$ modes. b, d, f) resulting normalized scattered light signals as a function of time. a, b) the fringe spacing d divided by the period of the normalized signal V yields the component of the velocity vector of the particle in the direction perpendicular to the interference fringes, $V_\perp$. c, d) the fringe spacing $\Delta\phi$ divided by the period of the normalized signal V yields the component of the velocity vector of the particle in the angular direction, Ω. e, f) if the particle orbit and the light are not concentric, interpreting the resulting normalized signal is not straightforward and requires an alternative approach.

Previous direct attempts to measure rotation in fluids fall into two classes: scattering of unpatterned light by specially engineered particles [18], and scattering of patterned or structured light by the same particles used for PIV and LDV [15,19]. In the first class, the vorticity (a measure of the local angular velocity) of small spherical particles with embedded planar mirrors are measured with a spatial grating system [18]. The spatial and temporal resolutions of this strategy are small (μm) and fast (ms). However, the environments in which measurements of this type can be conducted are limited, as matching the optical and physical properties of the seeding particles to those of the flow is required but can only be accomplished in specific cases. Moreover, fabricating the seeding particles is quite involved.

In the class of direct rotation sensors which illuminate readily available small particles with structured light, one approach calculates the fluid circulation by statistically analyzing the frequency shifts present in the scattered light when particles traverse a ring-shaped Laguerre-Gauss (LG) beam [19]. LG beams have phases which vary azimuthally as $\exp(il\phi)$, where i is the imaginary number, l is the azimuthal mode number, and ϕ is the azimuthal angle about the beam axis. LG beams also have radial modes indexed with p; here, all LG beams have $p = 0$. These beams possess $l\hbar$ of OAM. Because changes in phase give rise to changes in frequency, particles passing through such beams scatter frequency shifted light. The system of Ref. [19] was demonstrated using a flow field simulated on a digital micromirror device (DMD), and was found to estimate the vorticity with a spatial resolution of 0.1 cm. However, the statistical

Optics EXPRESS

signal processing technique requires many particle transits through the probe beam, and this limits the temporal resolution of the sensor. In the simulations from Ref. [19], for example, the transits of 250 particles were assembled for each measurement. The experiments from Ref. [19] were conducted in a highly controlled environment that allowed for frequency shifts to be measured via optical heterodyne, interfering the scattered light with a reference beam on the photodetector. In such a configuration, the probe and reference beam travel separately to the photodetector, with the probe beam traveling through the fluid and the reference beam bypassing the fluid. Consequently, the beams experience different environments could induce phase noise and beam steering, complicating detection in actual fluid applications.

An alternative approach for characterizing fluid rotation by measuring vorticity also uses LG beams to probe a seeded flow, but bypasses the challenges associated with the detection scheme of Ref. [19] by combining the signal and the reference beams before they enter the flow [15]. As such, optical modes remain overlapped and maintain their mutual coherence, even if features of the environment distort the wavefronts. The resulting beam has a petal-shaped interference pattern with $2l$ lobes. As the angular analog to LDV, this technique relates the frequencies of the intensity modulated scattered light to the angular spacing of the petal fringes to determine the angular velocities of the particles. The working principle of this sensor is illustrated in Fig. 1(c) and Fig. 1(d). However, two assumptions limit the applicability of this technique to more general flows. The first limiting assumption is that the particle orbits are concentric with the beam axis. This restricts where in the flow the sensor can function and makes the sensor sensitive to misalignment between the beam and rotating structures in the flow. The second limiting assumption is that the fluid moves obeying solid body rotation. The sensor always predicts the vorticity of the flow to be twice the angular velocity, even if the vorticity has contributions due to shear, meaning the flow behavior does not consist fully of the solid body rotation mode.

The sensor we present in this paper builds on the above approach, adding a more complex signal processing scheme in order to remove the limitations on which flow configurations it can be used with. As before, this is an Eulerian sensor, meaning that it remains fixed in the lab frame and it monitors the flow as it passes by. In our approach, we measure the angular velocity instead of the vorticity because in general cases, the Biot-Savart Law indicates that the velocities in a flow are due in part to contributions from both local and nonlocal vorticities [20] (See more on angular velocity versus vorticity measurements in the Appendix). We measure the angular velocity of a single particle embedded in a 2-dimensional flow (no velocity components in the direction of the probe beam) as it travels on a curved pathline and passes through a probe beam. Specifically, we model the pathline of each particle to be a circular arc, and we predict the particle's steady state angular velocity Ω along that arc. Approximating particle trajectories as curved can be justified by noting that many other flow velocimetry techniques assume particles travel only in straight lines. As in LDV, we sense this motion using a probe beam with interference fringes whose geometries are well characterized, and like the sensor of Ref. [15], these interference fringes are formed by conjugate LG beams having azimuthal modes $\pm l$. Also like these sensors, we make no assumptions about the viscosity of the fluid.

As we will explain below, while both LDV and Ref. [15] use frequency domain signal processing strategies, such an approach is not appropriate for the expected signals from this technique. The signal processing strategy which accompanies our angular velocity sensor requires characterizing each burst in the return signal resulting from the light scattered as a particle transits the probe beam and extracting a set of metrics with which we predict Ω. These predictions are conducted with a supervised machine learning regression model which is trained using experimentally validated simulated data. We expect that this sensor will function at short time scales defined by the duration of the particle transit as well as at short length scales set by the relative sizes of the particle and the transverse intensity profile of the probe beam. We anticipate that this sensor will find applications in systems which can accommodate only one optical access

Optics EXPRESS

port, where imaging techniques might not be possible, and where pathlines through probe beams cannot be approximated as linear.

The structure of the paper is as follows. In Sec. 2 we formalize the sensor, presenting the mathematical model we implement to simulate expected experimental signals. Experimental validation of these simulated signals is described in Sec. 3. With the simulated signals experimentally validated, we consider signals collected via simulations and experiments as interchangeable, and therefore are able to more flexibly and efficiently formulate and evaluate the signal processing strategy associated with the sensor using simulated results. The signal processing technique is discussed in Sec. 4. First, we describe the signal conditioning steps of the technique in Sec. 4.1. Then, in Sec. 4.2, we present the machine learning regression model at the heart of the sensor that predicts the angular velocity and orbit radius of particles. The results are discussed in Sec. 5. Sensor limitations are outlined in Sec. 6, where we pay special attention to the parameters which set the resolution of the sensor. Finally, we close with a discussion in Sec. 7, where we explain strategies extending the capabilities of the sensor to more complex fluid flows.

2. Sensor overview and simulations

In the case of LDV, the velocity component orthogonal to the interference fringes is given simply by the product of the distance d [L] between the fringes and the frequency at which the intensity of the scattered light varies [T^{-1}] (Fig. 1(a, b)). In the case of angular velocity sensing with conjugate LG beams, the distance from the LDV argument is replaced with the angular spacing $\Delta\phi$ [rad] [15] (Fig. 1(c, d)). However, if misalignment between the probe beam and the particle axis of rotation exists, as depicted in Fig. 1(e), the particle no longer traverses interference fringes spaced equally in angle, and the resulting time series no longer possesses a single temporal frequency that can be used in such an analysis. In fact, as shown in Fig. 2, particles can travel on orbits with the same radius and at the same angular velocity but yield very different time series if these orbits are centered at even slightly different locations. Thus, a more sophisticated signal processing scheme is required to predict the angular velocity Ω of the particle under the many possible combinations of orbit radii, centers of rotation, and angular velocities.

To train and validate our machine learning regression model for predicting the angular velocity and orbit radius of scattering particles traversing our probe beam, we numerically simulate the expected backscattered light that forms our data. In these simulations, we artificially sample an intensity petal pattern formed by interfering two LG beams with azimuthal modes $l = \pm 4$, radial modes $p = 0$, and a beam waist $w(z)$ with a minimum of $w_0(z) = 93.84$ pixels on a 986×616 pixel grid. These values were set to match the experiment that we use to validate the simulated signals, which is discussed in Sec. 3. Positions on the grid are referenced to its center using a radial coordinate system, $(\mathcal{R}, \phi)$.

The expected signal is modeled to be proportional to the scattered light from a particle. For simplicity, we model the scattering particle as a mirror oriented towards the detector, assuming that the particles have the same size, shape, and reflectivity so that the intensity of the light incident on the detector depends only on the intensity field at the particle location. Such assumptions are employed in the analogous technique of LDV [1] and are valid when the ratio of the spatial extent of the intensity pattern to the distance between the detector and the particle is small. Further, the simulated particles have identical radii of $r = 20$ pixels. Homogeneous seeding particles are readily available for fluid sensors due to advances in particle fabrication techniques [1]. In what follows, the size of the particle and the ratio r/w_0 remains unchanged and therefore is not necessarily optimized.

The simulated time series consists of signals from many particles passing through the petaled beam in series, with no more than one particle traversing the beam at a time. These passes are spaced in time to reflect a low density of seeding particles such that the time between transits is

Optics EXPRESS

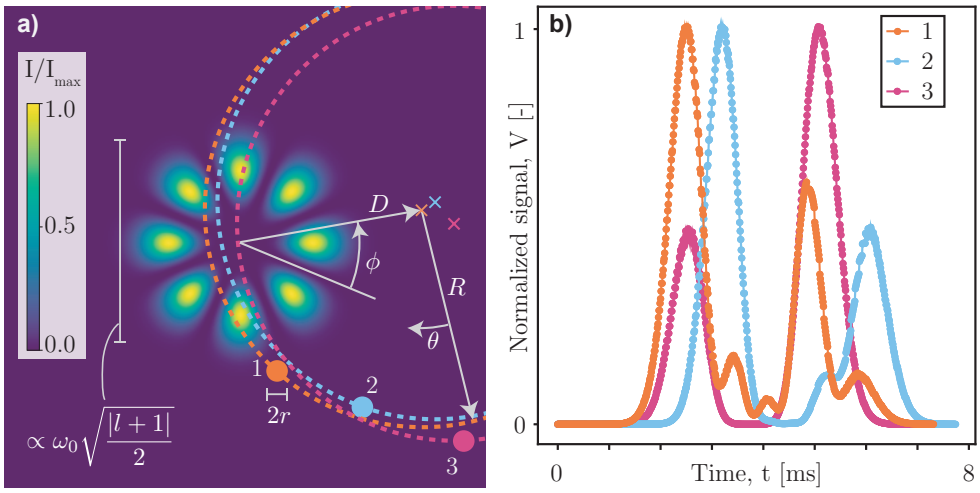

Fig. 2. Particle transit parameter space. A particle radius r travels on an arc radius R (broken lines) at an angular velocity $\Omega = d\theta/dt$. This orbit is centered at position (D, ϕ) (orbit centers marked with crosses) relative to the center of the interference pattern (normalized beam intensity simulated in background). As the particle passes through the interference pattern, it scatters light proportional to the intensity of light within the area of the particle. The size of the interference pattern is set by the beam waist, w_0, and the azimuthal index of the light, l. Three particles are shown as orange, blue, and gray circles. Each particle travels on an orbit of the same R at the same Ω , but the positions (D, ϕ) of these trajectories are slightly different. b) simulated time series for the particles shown in a), each normalized by its maximum value. Although the particles can all be considered to obey the same physics, the resulting signals are dissimilar due to where they cross the interference pattern. This illustrates the fundamental problem this sensor addresses, that particles which travel obeying the same physics, but which are probed at slightly different positions yield time series may not resemble each other. Parameters for particles 1, 2, and 3): $w_0 = 93.84$ pixels, $l = \pm 4$, $r = 20$ pixels, $R = 400$ pixels, $D = [340.3,\ 367.7,\ 396.6]$ pixels, respectively, $\phi = [-0.178, -0.205,\ -0.88]$ rad, respectively, and $\Omega = 250$ rad/sec.

at least as long as half the average time of a transit. As we will see in the signal conditioning step described in Sec. 4.1, spacing of approximately this time or longer is necessary for identifying the salient features of the signals.

The relevant particle transit parameters to this problem are illustrated in Fig. 2(a). We model the motion of each particle to have a constant angular velocity along a circular trajectory. The backscatter signal which results from a particle traversing the interference pattern is

$$\underbrace{V(t)}_{signal} \propto [\underbrace{g(\mathcal{R},\phi)}_{particle} * \underbrace{I(\mathcal{R},\phi)}_{intensity}] \times \underbrace{X(\mathcal{R},\phi,t)}_{trajectory} + \underbrace{n(t)}_{noise}, \tag{1}$$

where the particle is considered to be a perfect mirror using a *tophat* function $g(\mathcal{R}, \phi)$ equal to 1 within radius r and 0 otherwise. The particle functions as the kernel of a round blurring function which operates on the calculated intensity field of the interference pattern, $I(\mathcal{R}, \phi)$. The particle trajectory $X(\mathcal{R}, \phi, t)$ is centered at (D, ϕ) relative to the beam center. The blurred intensity is sampled as a function of time t along the trajectory of the particle at a sample rate of 100 kHz. We add white noise to the time series to generate the expected detector signal V.

Optics EXPRESS

The parameter space consists of 7 variables, $\{w_0, l, r, R, \phi, D, \Omega\}$, and is illustrated in Fig. 2(a). We reduce the dimensionality of the parameter space by fixing the characteristics of the light (w_0, l) as well as the particle radius (r). Additionally, we leverage the radial symmetry of the light to restrict ϕ, limiting the orbit center positions relative to the beam axis to angles $\pi/(2l) \leq \phi < 3\pi/(2l)$. At each (D, ϕ), where D is the distance between the orbit center and the beam axis, the orbit radius R is limited to values that allow the particle to pass through the petals of the interference fringes. Noting that the beam width at full width half maximum intensity scales by $r_p \sim w_0 \left(\frac{|l+1|}{2}\right)^{1/2}$ [21], this limitation constrains R to $D - r_p - r < R < D + r_p + r$. Any particle radius r on an orbit with radius R centered at (D, ϕ) relative to the beam axis, then, will travel through the interference fringes.

In Fig. 2 we plot the simulated signals corresponding to three particles traveling on orbits with the same radii at the same angular velocities, but with slightly offset orbit centers. Though the particles in each of these simulations move according to the same physics, the resulting time series appear to have no similarities. These traces emphasize the signal processing challenge of this sensor, which is to create a model which relates a set of metrics from these dissimilar signals to predict the same Ω.

In this section, we have presented LDV in its fringe configuration, but we note that LDV can also be operated in a heterodyne configuration, wherein the flow is illuminated with only one beam (no interference fringes) [22]. In this alternative setup, particles in the flow backscatter Doppler shifted light which interferes with a second (local oscillator) beam on the detector, and the velocity of the particles is related to the measured frequency shift. Likewise, the rotation measurements we present here could also operate in this alternative heterodyne configuration in which the flow would be illuminated with a single LG beam and then the backscattered light would interfere with a conjugate LG (local oscillator) beam on the detector. While the fringe and heterodyne optical arrangements are mostly equivalent [23,24], the fringe method that we detail in the paper provides an increased tolerance to scattering, as phase aberrations do not affect the overlap of the beams. The fringe method also eases the alignment constraints in the detection system. In our experience working with LG beams in the lab, we have found that obtaining sufficient modal overlap can be challenging. Knowing that passing only one of the two beams through a fluid environment would probably aberrate its wavefront, we have opted to mimic the fringe strategy.

Because simulations provide a more controllable environment than experiments, we use the simulations detailed in this section to develop and evaluate our sensor. We proceed by first ensuring that the simulations capture the important experimental features by comparing them to experimental results. This validation process is described in the following section. The code for the simulations detailed in this section and the analysis which follows are publicly available [25].

3. Experimentally validating the backscattered light simulations

To experimentally validate our simulations, we conduct highly controlled experiments and compare the results to our simulations with a cross correlation. While we have designed our sensor to be used in fluid flows, the proof-of-concept experiments we present here follow the strategy of Ref. [19] and replaces the fluid system with a digital micromirror device (DMD). This gives us precise control of the dynamics of the 'flow' and allows consistent repetition of a particular condition. Ultimately, this allows us to verify that, up to the assumptions outlined in Sec. 2, our simulations match our experiments. In the first subsection below, we present our experiment and discuss the experimental data acquisition process. In the second subsection, we describe the experimental validation strategy which we use to justify replacing experiments with simulations in developing the sensor.

Optics EXPRESS

3.1. Experimental setup

In Fig. 3(a) we present a schematic of our experiment. Using a HeNe (Thorlabs, HNL050LB) as our light source, we prepared a Laguerre-Gauss beam of light with $l = \pm 4$ using a spatial light modulator (SLM, Cambridge Correlators, SDE 1024). The SLM was programmed to display a computer-generated hologram consisting of a forked grating and a mask that selects only the $LG^{p=0}$ radial orders in each of the diffracted beams [26]. The first diffracted order was then isolated from the others with a spatial filter and directed towards a digital micromirror device (DMD, Texas Instruments, DLP4500). The DMD displayed a video of a small circle (radius 0.15 mm) traveling on a circular trajectory. These videos were designed so that no more than one particle passed through the light at a time. The video framerate was fixed at $f_{dmd} = 0.225$ Hz. The light sampled by this moving group of mirrors was collected on a photodetector (Thorlabs, Det36a). The resulting time series was low pass filtered (Mini-Circuits BLP-1.9+, 1.9 MHz cutoff frequency lumped LC low-pass filter) and then digitized with a data acquisition system (DAQ, National Instruments, USB6215) with a sampling rate of $f_s = 100$ kHz. Though the cutoff frequency of the low pass filter was greater than half the sampling rate of the DAQ meaning that aliasing could have occurred, the dynamics of the experiment (0.225 Hz) were far slower than either the cutoff frequency (1.9 MHz) or the sampling rate (100 kHz), so this was not a concern, and any data that was aliased was interpreted as noise.

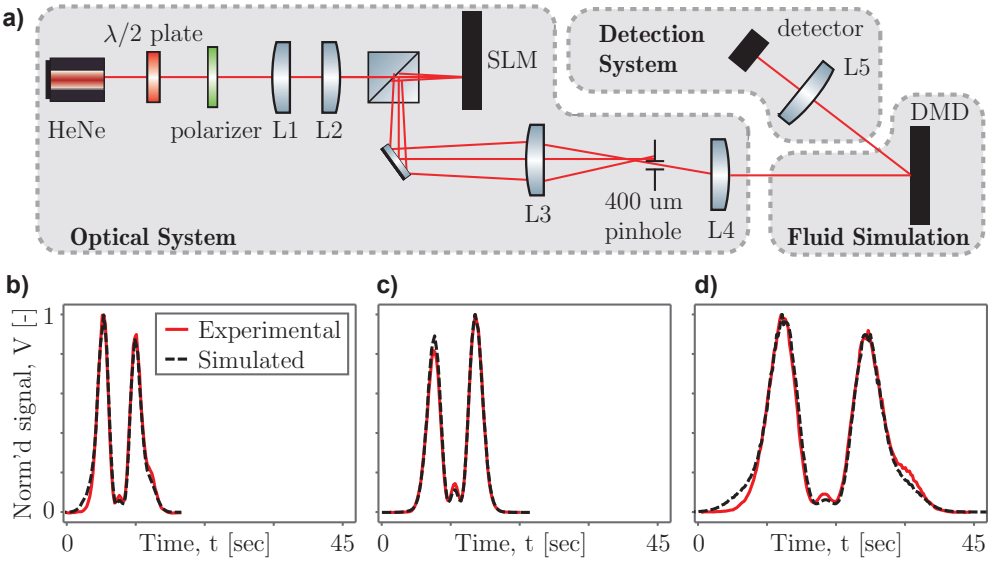

Fig. 3. a) Experimental setup. The optical system prepares the probe beam to be directed to the fluid simulation module by converting the Gaussian laser beam from the HeNe laser to a superposition of conjugate $\pm l = 4$ Laguerre Gaussian beams. The fluid simulation is conducted on a digital micromirror device (DMD). Simulated scatterers reflect light to the detection system, which digitizes the intensity of the light impinging on a detector, yielding the signal we analyze. $\lambda/2$: half wave plate, L1-5: lenses, SLM: spatial light modulator b-d) experimental (red solid lines) and simulated (black broken lines) normalized signals as a function of time. Parameters for simulations and experiments shown in b-d: $w_0 = 93.84$ pixels, $l = \pm 4$, $r = 20$ pixels, $R = 1200$ pixels, $D = [1250, 1265, 1250]$ pixels, respectively, $\phi = 0$ rad, and $\Omega = [654, 548, 223]$ rad/sec, respectively.

In principle, we could have run our experiments at a rate set by the ultimate speed of the DMD, 4225 Hz. However, because the objective of these experiments was to generate data with which to

Optics EXPRESS

validate our simulations, we opted to operate at a fraction of this speed so that we could average the signal at each frame to improve its signal to noise ratio (SNR). Each video frame played for $f_{dmd}^{-1} = 4.44$ seconds, and the voltage corresponding to the intensity of the light impinging on the photodetector for that frame was calculated using the signal from the middle 4 seconds of data. Prior to averaging, we applied a numerical Butterworth filter (5th order, cutoff frequency 50 Hz) to the signal for smoothing. These steps increased the SNR by reducing the effects of noise arising from the influence of the multimodal nature of the laser as well as the noise induced by circuitry implemented to support the DAQ. The SNR, calculated as the ratio of the mean and the standard deviation of the numerically smoothed signals, was found to be, on average, 42.

We designed the DMD videos so that the averaged signal would correspond to the motion of a particle traveling on an arc with a specific angular velocity, sampled at f_s. The particle position was calculated such that it moved along its arc by an angular spacing $\Delta\phi = f_s/\Omega$. Because f_s was fixed, we varied the angular velocity of the experiments by changing the angular spacing between the frames.

3.2. Comparing signals from simulations and experiments

We conducted 47 experiments to validate our simulations varying D and Ω ($1150 \leq D$ [pixels, 10 values] ≤ 1305, and $223 \leq \Omega$ [rad/sec, 7 values] ≤ 655) while fixing the remaining parameters at the following values: $w_0 = 93.85$ pixels, $l = \pm 4$, $r = 20$ pixels, $R = 1200$ pixels, $\phi = 0.0 \pm 0.01$ rad. Examples of the experimental results compared to their simulated counterparts are shown in Fig. 3(b-d). To assess the similarity of the experimental and simulated signals, we calculated the maximum cross correlation, normalizing it by the autocorrelation of each of the signals at zero lag: $\max(\hat{R}_{xy}) = \max\left(\left(R_{xx}R_{yy}\right)^{-\frac{1}{2}} R_{xy}\right)$, where

$$R_{xy}(m) = \begin{cases} \sum_{n=0}^{N-m-1} x_{n+m} y_n^*, & m \geq 0 \\ R_{yx}^*(-m), & m<0 \end{cases} \tag{2}$$

for $-\infty<n<\infty$, $m>0$, N being the length of the longer signal x or y, and where * represents the complex conjugate. We find high correlations between the simulated and experimentally collected signals, with the mean and the standard deviations of the correlations of each of the 47 experiments with its corresponding simulation being 0.96 and 0.03, respectively.

As discussed above, our simulations were constructed with a discretization selected to match the pixelation of the DMD, with pixels in both cases being square having widths $s = 7.637$ μm [27]. Projecting the radial pattern on the square grid created the possibility that the pixel orientations were rotated relative to each other, and this could have an influence on the calculated and measured intensities. However, because the particle is large relative to the pixels ($r/\ s = 20$) and blurs the intensities from every pixel within it, we found this effect to be negligible. As seen in Fig. 3(b) and Fig. 3(d), the agreement between the simulation and the experiment appears to break down when the particle starts and finishes its transit through the light. We believe this is due to imperfections in our beam. The holograms displayed on the SLM were generated assuming the incident beam was Gaussian in intensity, but a beam profiling system (WinCamD LCM, DataRay) indicated that a Gaussian fit to the intensity of the beam at its centroid by iteratively adjusting its height and width deviated in its integrated area from that of the beam by approximately 7%. Such deviations in the incident beam would propagate through the hologram and manifest as unexpected intensity variations in the LG beam. This could be related to the same features which led to the discrepancy between the experimental and simulated intensities shown in Fig. 3(b) and Fig. 3(d). Noting that these discrepancies were small and anticipating such variations between experiment and simulations due to the complexities associated with directing light into a fluid, we decided that because the maximum cross correlation between the

Optics EXPRESS

experimental and simulated signals was higher than a threshold we set of 0.90, that we would proceed with the sensor demonstration.

4. Signal processing

The signal processing algorithm consists of two modules: signal conditioning and angular velocity prediction. The conditioning step begins by first identifying which portions of the signal contain information from a particle transiting the interference pattern. Only small portions of the signal which we call *bursts* contain information. These bursts correspond to the transit of a particle through the probe beam. In our signal processing scheme, we first isolate these bursts and then parameterize them by fitting with multiple Gaussian functions. The resulting parameters are used as the inputs for the machine learning (ML) model, which predicts the angular velocities and orbit radii of the trajectories of the particles. This ML model is pre-trained using data generated via the simulations described in Sec. 2.

In the present section, we outline the signal conditioning we apply to the all of the data, first discussing the details of the burst detection scheme and then moving on to describe multi-Gaussian fit step. We note that all data, be it experimental or simulated, for model development or evaluation, is processed identically following the steps outlined here. We close this section with a discussion of the architecture of the machine learning model.

4.1. Signal conditioning

The time series data associated with these experiments is both intermittent and aperiodic because particles transit the beam unpredictably while the data acquisition system runs continuously. The challenge is to first determine which portions of the time series correspond to bursts, transits of scattering particles through the beam, and then to extract information from these bursts by parameterizing them.

4.1.1. Burst detection

A particle passing through the interference fringes scatters light proportionally to the intensity of the light incident on the particle. When the particle is positioned within a null of the interference pattern, no light is scattered at all. Therefore, a burst may contain valleys of only noise between high intensity regions. Consequently, bursts cannot be detected directly with a zero-crossing algorithm, as this may errantly split a single burst into many. Instead, we smooth the signal by convolving it with a *rect* function whose width is greater than the expected duration of the longest null. We then use a crossing algorithm to determine when a burst starts and finishes by comparing this smoothed copy of the signal to a threshold set by the convolution of the *rect* with a portion of the signal which consists of only noise. To ensure we select the entirety of the burst without clipping any information, buffering regions which we call *tails* are added to the beginning and end of each burst. Though these tails contain little or no information about particle movements, they can have an influence on the burst parameterization. To prevent artifacts from the burst detection scheme in later stages of the analysis, the tail durations of each burst are selected at random within a range that keeps the tail small relative to the total burst duration.

4.1.2. Multi-Gaussian fits

Once we identify the bursts, we parameterize them to summarize their dominant features for use as inputs to the machine learning (ML) model. In principle, the time series of the burst itself could be directly input to the ML model, but we found that this approach was highly sensitive to the length of the tails of the burst which contain little or no information. Therefore, we used a curve fitting scheme to parametrize and extract the features from the burst.

One parameterization strategy that is commonly used by optical sensors involves using a Fourier decomposition. However, such an approach proved futile here because the bursts have

Optics EXPRESS

relatively little periodic behavior. Moreover, sinusoidal basis functions are continuous in time, whereas the bursts are discrete and localized in time. Due to the periodic nature of Fourier decompositions, such a parameterization would have a strong dependency on the length of the tails of the bursts. Therefore, we opted for an alternative parameterization technique which incorporated basis functions which trend to zero away from their maxima, more closely resemble the bursts, and deemphasize the lengths of the burst tails.

In this paper, we parameterize the bursts with a sum of multiple Gaussian functions and a small vertical offset which allows for noise. Noting that a burst corresponding to a single pass of a particle through the interference pattern should contain no more peaks than petals in the interference pattern, we sum up to $2l$ (here, $2l = 8$) of these Gaussian functions as follows:

$$y = h + \sum_{n=1}^{2l} A_n \exp\left[\frac{(\mu_n - t)^2}{\sigma_n^2}\right]. \tag{3}$$

In this sum of Gaussian functions, A, μ, and σ are the amplitude, temporal offset, and width of the Gaussian functions, respectively, and h is a vertical offset. Examples of bursts fit in this way are shown in Fig. 4. We note that alternative orthogonal decompositions with compact support like wavelet transforms might also provide a means for this processing step.

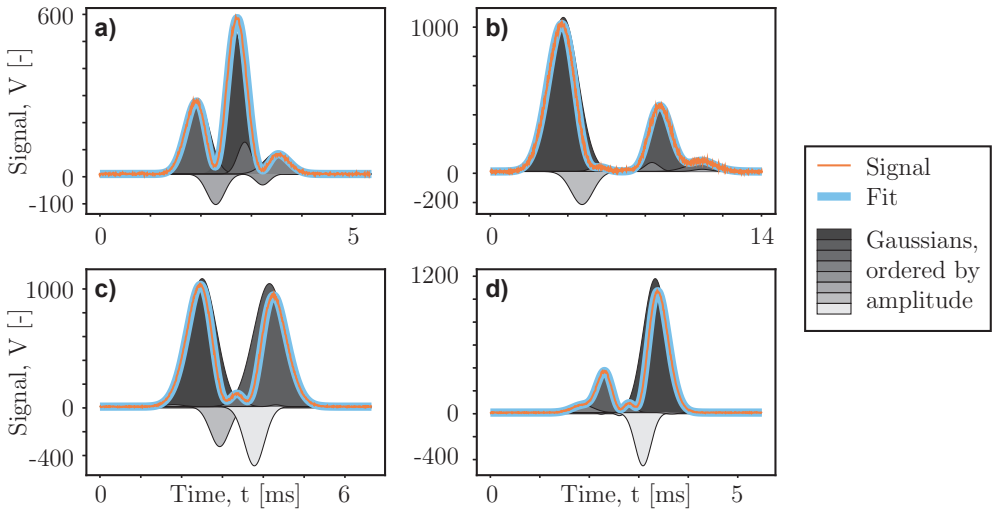

Fig. 4. Bursts parameterized by fitting Eq. (3) to them. Each of the fitted Gaussians is shaded with a color corresponding to its amplitude. Parameters for bursts in a, b, c, and d: Ω = 284.4, 100.4, 346.3, 268.5 rad/sec, R = 535.9, 435.9, 312.1, 608.2 pixels, D = 362.5, 391.0, 379.7, 670.9 pixels, and ϕ = 0.64, 0.51, 0.76, 0.94 rad. In all cases, r = 20 pixels and l = ±4.

Gaussian functions do not form an orthogonal basis, so a great deal of care was taken to ensure that the parameterizations converged to realistic and physical solutions. Curve fits were performed sequentially on each burst. The vertical offset was initialized as the noise level of the signal. Initially, a peak finding algorithm identified the number and locations of the local maxima of the burst. If there were fewer than $2l$ peaks, the first fit was conducted with Gaussian functions positioned at each maxima. These Gaussian functions each had an amplitude A equal to the difference of the burst value at that position and the noise level, and widths σ calculated to be 1/10 the rect effective width of the signal, calculated by numerically integrating the difference

Optics EXPRESS

between the signal and the noise level, then dividing this quantity by the maximum amplitude of the difference between the signal and the noise level. Fits were weighted with smoothed copies of the bursts to emphasize the portions corresponding to the signal while simultaneously deemphasizing the tails. If the residuals between the resulting fit and the signal were greater than a threshold set by 110% of the noise level, a new fit was conducted, this time with a new Gaussian function at the position of the residual with the largest magnitude. As before, the previously placed Gaussian functions were located at the peak positions with parameters set by the peak at that location. The newest Gaussian function was now permitted to have a negative amplitude. We iterate this process until either the magnitude of the residuals was smaller than the noise floor, or until more than $2l$ Gaussian functions were necessary. Though in some cases the Gaussian functions were found to have significant overlap to characterize a single peak in the burst, we set the threshold to be equal to the number of petals in the interference pattern ($2l$, which is 8 here) based on the intuition that the signal would not have more peaks than petals. If more than 8 Gaussian functions were needed to parameterize the signal, or if the fits failed to converge at any step, the burst was eliminated. Approximately 80% of our bursts had fits which converged with 8 or fewer Gaussian functions in the parameterization. The remaining 20% of the bursts which appeared to have no common features with each other were discarded.

4.2. Predicting angular velocity and orbit radius with a machine learning model

A machine learning regression algorithm allows us to discern correlations between the angular velocities of the rotating particles and parameterizations of their resulting bursts. The machine learning model used in this paper is built using APIs from the open source software libraries Keras [28] and TensorFlow [29]. The model is a sequential model with two densely connected layers which use the rectified linear unit (ReLU) nonlinearity and an output layer which returns two continuous values, Ω and R. The predictions of R have large uncertainties so we do not consider them to be a part of our sensor, but we include them in the quantities the model predicts because they improve the fidelity of predictions of Ω. As an input, the model takes the parameters of the bursts described above, as well as several additional parameters characterizing the duration of the burst and the quality of the fit. The amplitudes A_n of each burst are normalized to the largest A_n of the burst. This serves to permit fluctuations in the intensity of the probe beam on time scales longer than the duration of the burst. In order to remove the influence of the tail length, the temporal offsets μ_n are referenced to the earliest μ_n parameterizing the burst. To ensure all parameters are equally represented in the model and to stabilize the training, each variable is independently scaled to approximately the same range ([0,100]) based on the minimum and maximum expected values based on the properties of the experiment and the flow. Identical normalizing factors were used in model training and evaluation. The model has 6,210 trainable parameters which are trained by minimizing the mean square error using the RMSprop optimizer. To avoid overfitting, the model is trained with an EarlyStopping [29] callback that halts the training when little improvement is seen in the validation error. Training data is also augmented by fitting up to three copies of each burst, each padded with tails of different length. In total, 83,885 parameterizations of 51,182 bursts are used to train the model. These bursts correspond to simulations conducted with the following parameters: $300 \leq D$ [pixels]≤ 700, $100 \leq R$ [pixels]≤ 920, $50 \leq \Omega$ [rad/sec]≤ 1040, $\pi/8 \leq \phi$ [rad]$\leq 3\pi/8$.

5. Results and discussion

Once the machine learning model was trained, it was evaluated with a second set of parameterizations of 2,948 bursts selected independently and at random within the same parameter range as the training set. The results are shown in Fig. 5, where we plot the predicted angular velocity, Ω_P, as a function of the actual angular velocity, Ω_A. The results are binned into 25 angular velocity partitions of width 39.5 rad/sec.

Optics EXPRESS

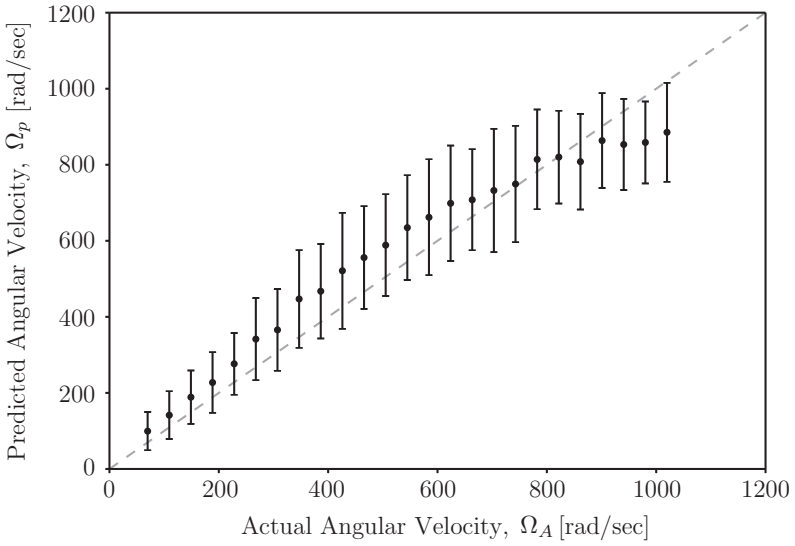

Fig. 5. Predicted angular velocity as a function of actual angular velocity. 2,948 bursts with varying R, ϕ, D, and Ω sampled in the ranges described in the text are used to evaluate the machine learning model. The mean (closed circles) and standard deviation (uncertainty bars) of predicted angular velocities are plotted for each of the 25 partitions of width of 39.5 rad/sec of the sampled angular velocity range. Each partition contains predictions for more than 70 bursts.

This sensor has a dynamic range of $50 \leq \Omega_A$ [rad/sec] $\leq\approx 800$, wherein Ω_P scales linearly with Ω_A.The limit of linearity of the sensor beyond which this sensor no longer provides useful predictions of Ω_A is $\Omega_A \approx 800$ rad/sec. Though we found that the limit of linearity was always smaller than the ultimate angular velocity used to train the model, we were unable to attribute this observation to physical characteristics underlying the simulations. Therefore, we recommend training the model with simulations which have angular velocities larger than those expected in the experiment.

Within the dynamic range of the sensor, the mean measured Ω_P is biased and systematically over predicts Ω_A; however, this effect could be calibrated by subtracting the average bias from the prediction since the model is evaluated with "known" simulated reference standards. In this demonstration, we forgo such a calibration step in an effort to emphasize the ML component of the signal processing algorithm. After such a calibration step, the resulting predictions would still retain the dispersion shown in Fig. 5 but with no bias. We define the measurement uncertainty as the standard deviation of the angular velocity predictions within each angular velocity prediction since this dispersion relates directly to the quality of the measurement. As indicated with uncertainty bars in Fig. 5, the measurement uncertainty is a function of Ω_A, but is no more than 162 rad/sec for $\Omega_A \leq 800$ rad/sec. The uncertainties are, on average, $\pm 14\%$ for each burst.

We expect that the uncertainty discussed above has two dominant sources, (1) the geometry of the sensor, and (2) burst parameterizations. In the first case, the radial symmetry of the probe beam and the circular trajectories of the scattering particles can conspire to generate very similar bursts with multiple parameter combinations. An example of this situation is illustrated in Fig. 6, where the simulated trajectories of particles with different orbit centers, orbit radii, and angular velocities are shown to yield almost identical bursts. Given the parameterization of one such burst, the model may ascribe an incorrect angular velocity to the burst that is not uniquely generated by one set of values of the underlying parameters. The other dominant source

Optics EXPRESS

of uncertainty arises as a consequence of the non-orthogonal basis functions used to fit the burst: many parameterizations of the same burst exist.

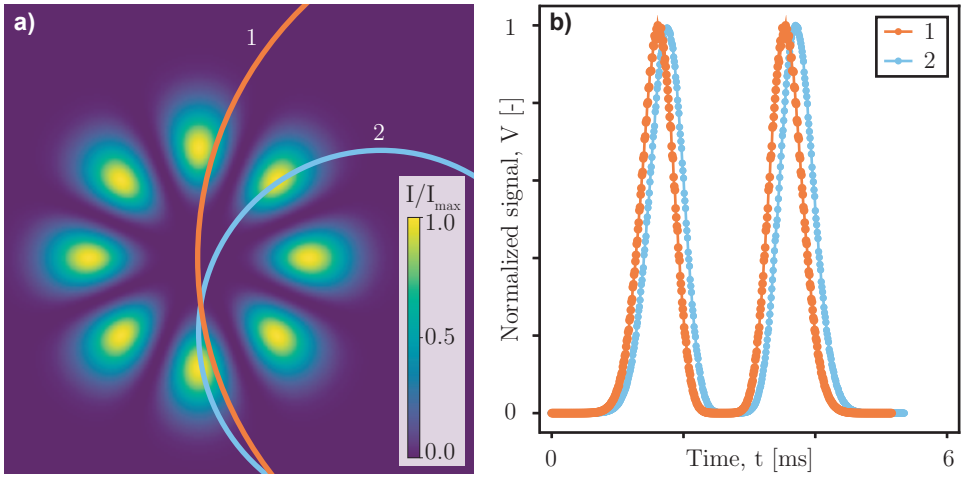

Fig. 6. Particles traveling with different angular velocities on orbits of different sizes can generate similar signals. a) particle trajectories with 1: $\Omega = 600$ rad/sec and $R = 426$ pixels and 2: $\Omega = 312.5$ rad/sec and $R = 220$ pixels. b) simulated time series for particle trajectories shown in a), each normalized by its maximum value. Traces offset by 0.12 ms for clarity. Parameters for trajectories 1, 2: $D = 425,\ 238$ pixels and $\phi = 0.393,\ -0.005$ rad. In both cases, $r = 20$ pixels and $l = \pm 4$.

In this proof-of-concept demonstration, we have chosen to sacrifice uncertainty for simplicity. Nonetheless, we have identified several ways to reduce the uncertainty of the measurements. We expect that the contribution to the uncertainty from the non-orthogonal basis functions can be refined by training, evaluating, and using the model with multiple parameterizations of each burst. One approach to improve the uncertainty of the sensor due to the geometry is to first determine which bursts can be generated by more than one set of orbit centers, orbit radii, and angular velocities, and then to exclude these bursts from analysis by preventing their use in training the model and by rejecting them from being evaluated by the model. An alternate approach is to limit the parameter range used to train the model to a narrow window centered about the expected flow conditions.

A different strategy to improve the uncertainty of these measurements is to modify the illumination beam, optimizing it so that non-unique signals are not generated in the first place. Building on the previous work of Refs. [15,19], we developed and tested this signal processing toolbox using a probe beam consisting of conjugate LG beams which formed a petaled pattern. However, we expect that better spatially structured beams could be optimized to augment angular velocity predictions. For example, an asymmetric pattern could be used to reduce the set of possible parameter combinations that can generate any given signal and to disambiguate direction. Further direction disambiguation could be accomplished by structuring the polarization field [30].

In this study, we have fixed the size of the scattering particle with a radius $r = 20$ pixels. Recalling that the scattering particle acts as a blurring filter, changing its size to smooth different amounts of the beam may serve as a means for tuning the uncertainties discussed above. Likewise, increasing l might reduce the number of non-unique bursts.

When using this sensor in a flow which evolves more slowly than the time it takes to conduct multiple measurements, the uncertainty of the angular velocity could be further refined with

Optics EXPRESS

a statistical treatment of the predicted angular velocities using a Student's t-test since the distributions of Ω_p about Ω_A are well approximated with normal distributions.

In this demonstration, we extended the traditional capabilities of laser Doppler velocimetry by developing a signal processing toolbox which predicts the angular velocity of a particle traveling on a circular orbit using a machine learning approach to develop a model to relate parameterizations of a signal to the angular velocity. This strategy was shown to be particularly effective in predicting the angular velocities of small particles traveling on circular orbits, where no one-to-one relationship existed between characteristics of the scattered light signal and the spatial pattern of the illuminating beam. We also point to the possibility of predicting related or different kinematic quantities such as the location of the orbit center or accelerations with a similar machine learning-based signal processing scheme.

6. Current sensor limitations

As with any sensor, we expect this angular velocity sensor to function only within a certain parameter range. In this section, we first discuss why this sensor is capable of measuring the angular velocities of particles moving only along arcs with radii below a critical radius set by the size of the interference patterns. Next, we discuss the minimum and maximum angular velocities we expect the sensor to be able to resolve. Additionally, we describe the spatial and temporal resolutions of the sensor. Then, we touch on the physical limitations which set the beam size and the particle size. Finally, we discuss how this measurement has no depth resolution.

6.1. Orbits require curvature through interference fringes

As the orbit radius R grows large relative to the interference fringes, $R \gg w_0\sqrt{|l+1|/2}$, the particle trajectory becomes increasingly well approximated using the first order, straight line tangent to the arc. We call this trajectory R_∞. This concept is illustrated in Fig. 7(a), where we show particle trajectories of several radii, all passing through the same point with the same tangent velocity, $V = 2\pi R\Omega$. As R grows, much of the particle trajectory through the interference fringes mimics that of the tangent, and only as the particle first enters and finally exits the interference fringes do deviations of the trajectory from that of the tangent appear. In the inset of Fig. 7(b) we plot the time series which correspond to the trajectories plotted in Fig. 7(a). We see that as the orbit radius approaches the tangent line ($R \to \infty$), the signals begin to resemble each other.

When $R>R_c$, where R_c is the critical orbit radius above which curvature in the trajectory is negligible, the values of R and Ω become ambiguous. That is, the tangent velocity could be the product of any $R>R_c$ with a compensating angular velocity Ω to yield V. Therefore, we expect our sensor to function only for $R<R_c$.

The specific value of R_c is a function of r, l, w_0, D, and ϕ. Instead of calculating R_c we use the normalized cross correlation R_{xy} defined in Eq. (2) to compare bursts from a set of simulated particle trajectories which pass through the same point within the interference pattern but have orbits with different R to the burst corresponding to the tangent trajectory through the common point. In this normalized cross correlation, x and y represent time series corresponding to the trajectories with orbit radius R and R_∞, respectively. To facilitate this comparison, all particles pass through the common point with the same tangent velocity V calculated as $V = \Omega/(2\pi R)$ for $R \neq R_\infty$. Because the orbit curvature of particles on transits with $R>R_c$ is negligible through the interference pattern, the normalized cross correlation of bursts corresponding to these conditions with the burst of the tangent case is close to 1. The influence of nonnegligible orbit curvature manifests as a difference in the beginnings and ends of a burst and results in a normalized cross correlation less than 1. The results of this comparison are shown in Fig. 7(b) as a function of R. To emphasize the strong dependence of this function on D and ϕ, R_{xy} is plotted for several different common points with different tangent angles. We define R_c as the radius at which R_{xy} is greater than 0.98. In the case of the data shown in Fig. 7, $R_c \approx 1000$ pixels.

Optics EXPRESS

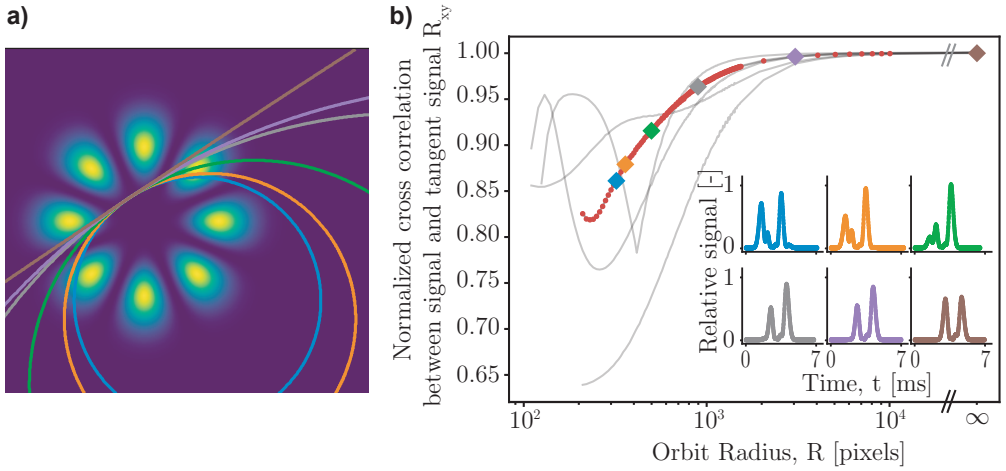

Fig. 7. a) As the orbit radius R grows, the trajectory of a particle moving through the interference fringes approaches that of the tangent to the arc. Colors of trajectories match those in panel b) and correspond to orbit radii $R = [200, 260, 400, 900, 1210, \infty]$. All arcs pass through $(50, 5\pi/16)$, and all arcs share the tangent shown in brown. b) Normalized cross correlation R_{xy} between each signal and its corresponding tangent. Each gray line corresponds to R_{xy} for sets of arcs passing through several randomly chosen different common points. The gray line with red circles corresponds to the common point illustrated in panel a). Inset: signals corresponding to those in panel a) and indicated with colored diamonds in panel b).

In principle, the angular velocity of a measurement which predicts $R>R_c$ should not be accepted because of the ambiguity between $R>R_c$ and Ω discussed above. To avoid needing to reject measurements in our proof-of-concept sensor demonstration, we estimate that $R_c \approx 1000$ pixels at every point, and we use only $R<1000$ pixels in both the training and test data to eliminate any trajectories which might resemble the tangent trajectory.

6.2. Sensor resolution

As the angular velocity increases, the number of sampled points per burst decreases for a fixed sampling rate. With fewer data points, the number of degrees of freedom in the burst parameterization fits decreases. As the number of degrees of freedom decreases, so too does the quality of the fit. At a minimum, these fits require the same number of points as there are parameters, which here is $3 \times 2l + 1 = 25$. However, we found that when bursts had fewer than approximately 50 points, the fitting scheme was sensitive to noise in the burst. Therefore, we established a criteria for selecting fits for use in training or testing the machine learning model which controlled the quality of the fit, accepting fits only if their coefficient of determination $r^2>0.9$, meaning that the model explained more than 90% of the variation in the burst. For a given trajectory, increasing the sampling frequency increases the number of points in the burst, so the angular velocity range can be tuned by modifying the sampling frequency.

The temporal resolution of each measurement is given by the duration of the burst: $\delta t = t_{burst}$. An upper limit of the time resolution can be estimated from the time it takes a particle orbiting with the smallest angular velocity along the smallest orbit to traverse the widest portion of the beam, $\delta t_{max} \approx 2r_p/(R\Omega)$. Figures 1, 2, 4, 6, and 7 have t_{burst} on the order of 10 ms. Increasing the angular velocity refines the temporal resolution.

Optics EXPRESS

We define the spatial resolution of the sensor δx to be the distance between the probe beam and the center of orbit of the particle. Given a particular center of orbit (D, ϕ), δx is limited by $D - r_p - r < \delta x < D + r_p + r$ since only orbits which transit the beam are measurable. The upper limit of the spatial resolution is approximated by $\delta x_{max} \approx D_{max} + r_p + r$, where D_{max} denotes the furthest center of orbit from the beam of light about which particles traverse the beam on trajectories with $R < R_c$. The spatial resolutions of the bursts described above are approximately $\delta x_{max} \approx 1500$ pixels = 1.45 cm.

6.3. Physical limitations to probe size

In this demonstration, we have fixed the sizes of both the particle and the interference pattern while we have varied the other parameters with the goal of predicting the angular velocity and the orbit radius of a particle embedded in the flow. However, both the particle size and the interference pattern size can be changed.

As in other velocimetry sensors which use scattering particles, particle radii r should be set by the parameters of the flow such that the particles are neither too small to have motion dominated by Brownian motion nor too large to carry enough inertia to travel along paths which are not fluid pathlines [1].

The scattered light must have ample power to be distinguished from noise by the detector. This power is limited by the intensity of the incident beam, which, given a laser source can be limited by two factors, the efficiency of reshaping the Gaussian intensity profile from the laser to the requisite LG modes, and the ultimate size of the beam. When an LG beam is generated from a beam with a Gaussian intensity profile and a fixed beam waist w_0 using an SLM as was done in this project, the efficiency of the diffraction gratings decreases as l increases due to the decreasing spatial overlap between the input and desired mode [21]. The transverse spatial extent of the generated LG beam can be altered using a telescope setup after the SLM. As the size of the beam increases, its total power remains constant, so the power incident on the scattering particle diminishes.

We expect that the smallest beam size possible is limited by the visibility of the fringes, the ratio of the intensities of the radial peaks and nulls. As the beam size decreases past approximately the wavelength of the light, this visibility decreases, and the fringes appear to bleed into one another [31]. Though we did not study its effect in this paper, we expect this decreased visibility to directly impact the sensor resolution by decreasing the sizes of the features in the bursts.

The ratio of the particle to interference pattern sizes is very important to the behavior of this sensor. Recall that the particle acts as a blurring function on the interference fringes. If the size of the particle is such that it occupies one fringe and one null of the interference pattern, one can imagine how moving the particle through an intensity peak, into an intensity null, and back through a different intensity peak would decrease the contribution to the blurred intensity from the waning edge while symmetrically increasing the contribution to the blurred intensity from the waxing edge, resulting in little signal modulation. In the case of laser Doppler velocimetry, the problem of selecting relative interference fringe and particle sizes to maximize the signal to noise ratio has been studied extensively [1]. While we did not study the effect of relative sizes in this paper, we do expect this to be an important parameter for designing specific implementations of this sensor.

6.4. Depth of measurement

The sensor we have demonstrated has no longitudinal sensitivity. That is, the scattered light we measure contains no information regarding the depth of the particle. We expect that in future iterations of this sensor, this limitation could be lifted by incorporating a confocal sectioning geometry into the probe beam, by relating the absolute scattered intensity to the absorption of the fluid which scales linearly with depth according to Beer's Law, or by selectively seeding the flow.

Optics EXPRESS

7. Conclusion and future work

In this paper, we have developed a sensor which uses structured light and machine learning to predict flow properties. Specifically, we have demonstrated that we can calculate the angular velocity of particles traveling in a 2D flow along circular arcs by analyzing the intensity of the light they scatter. In laser Doppler velocimetry, the analogous technique used to sense linear components of the velocity vector, these components are directly related to the spatial and temporal frequencies of the illuminating interference fringes and the scattered light. In contrast, no simple mapping from the spatial pattern of the light and characteristics of the signal exists for predicting the angular velocity with this sensor. However, a machine learning regression model trained on simulations of the expected scattered light was shown to be capable of predicting the angular velocities of scattering particles to within uncertainties of, on average, ±14%. While many possible probe beam conformations exist, we have explored just one geometry. We suspect that other flow properties can be inferred using different probe beams with a similar signal processing scheme to the one presented here.

In Sec. 2 we presented mathematical model we implemented to simulate the expected signals. In Sec. 3, we described idealized experiments to validate the simulations. In Sec. 4, we detailed our signal parameterization approach, noting that because the Gaussian basis functions we used were not orthogonal, the resulting parameters had strong dependencies on how our fits were initialized. Consequently, the ML model was trained using particular instances of many possible parameters. Because the ML model was able to handle this variability, we suspect that our sensor would still function in more complex experimental environments which may induce random intensity fluctuations in the resulting signals. Such effects might mirror the effect of the non-orthogonal basis functions, both inducing a degree of variability on the output parameters. Here, by using non-orthogonal basis functions, we artificially introduce variability into the ML model, and we suspect that this facilitates studying noisier signals.

There remain ample opportunities for refining this sensor. We attempted to adapt the ML model to simultaneously predict combinations of variables in addition to the angular velocity, but we found that these predictions were poor. One interesting direction is to design the ML model to return a probability distribution of the possible angular velocities instead of a single value. Because the uncertainties associated with non-unique bursts arising from the multiple parameter configurations like that illustrated in Fig. 6 are restricted to quantized values, the outputs of such a model could be compared to physical intuition or multiple measurements to refine the selected angular velocity.

We expect that with a different structured light pattern, predicting such quantities as the direction in which the particle orbit is centered might be possible. Also, probing the flow with multiple, potentially multiplexed, light patterns could provide additional information to improve precision and accuracy or open up a broader range of parameter prediction. This could be done either simultaneously by multiplexing several patterns on beams with different polarizations or wavelengths, or by changing the patterns as a function of time.

The sensor we developed predicts the angular velocities of particles traveling on circular orbits in a plane orthogonal to the probe beam but in its current implementation does not allow for this plane to be positioned at a different angle relative to the beam. If the beam and the plane of orbit were not orthogonal, the particle would no longer appear to travel with a circular orbit and would instead take an elliptical trajectory through the beam. To extend our sensor to 3D, we anticipate that the longitudinal Doppler shift of the scattered light [32] could be incorporated into the ML model.

In its current form, the sensor we present in this paper measures angular velocities. Measurements of angular accelerations may also be of interest. Such measurements could be possible if the particle accelerated on, or faster than, a time scale set by the residence time (the time the particle is in the probe volume), $\tau \approx 2r_p/U_\perp$, where $U_\perp = \Omega R$. While the rotational Doppler

Optics EXPRESS

shift has been used to measure angular accelerations by creating spectrograms which monitor the frequency shift as a function of time [33], we expect that adapting such a paradigm to this problem would be challenging due to the short expected residence times. Expanding the parameter space of the machine learning model to include accelerating particle trajectories might be a more viable strategy.

In cases of simple motion like particles moving in straight lines or particle orbiting about a known point on circular trajectories, structured probe beams can be engineered which yield readily interpretable signals [10]. Here, we have attempted to address the question of what are we to do when the motion we expect is more complicated? In particular, we have studied particles which orbit according to circular trajectories, but these orbits are not concentric with the probe beam. The sensor we have developed measures the angular velocities of particles obeying such circular trajectories offset from the probe beam axis. We have accomplished this by developing a more sophisticated signal processing strategy. We have shown that, even if the motion and the structure of the light no longer match, a history of the particle's kinematic information can be revealed from the information encoded in the signal. However, we have found that a new form of uncertainty which previously did not exist is present in this more general case because signals may no longer uniquely correspond to the parameters of interest.

As we noted above, this uncertainty can be overcome by excluding signals like those shown in Fig. 6 known to have multiple possible origins, by refining the machine learning model, or by illuminating the flow with multiple, potentially multiplexed, light patterns. However, we must ask, if there does not exist a single pattern of structured light which can provide signals which are easy to interpret, does there exist some optimal probe beam structure? To begin to offer an answer to this question, we draw an analogy to the field of compressive sensing. A major finding which has propelled the field of compressive sensing in recent years is that samples of sparse signals collected as the inner product of random vectors with the signal can, with high probability, reconstruct the signal nearly perfectly [34]. This is because sampling randomly in this way spreads the information contained in the signal efficiently across many of the measurements. Likewise, we expect that illuminating the fluid with a known but random structure of light could encode bursts with more information by which to identify the parameters which generated them. Ultimately, combining such an illumination pattern with a machine learning-based signal processing scheme might facilitate more precise measurements.

Appendix

Angular velocity and vorticity

Particles orbiting a point move according to two modes: solid body rotation flow and free vortex flow. In the former case, the orientation of the particle (the direction the particle points) remains fixed about the center of rotation throughout the trajectory of the particle. In the latter case, the orientation of the particle remains unchanged relative to a stationary point as the particle moves. In these cases, the steady state angular velocities of the particle about the axis of rotation can be expressed as $\vec{\Omega} = [0, 0, \Omega]^T$ and $\vec{\Omega} = [0, 0, \alpha r^{-2}]^T$, respectively, where Ω is the angular velocity, α is a constant, and r is the orbit radius. The vorticity is calculated as the curl of the velocity, $\vec{\omega} = \vec{\nabla} \times \vec{U}$, where the velocity is given by $\vec{U} = \vec{\Omega} \times \vec{r}$ given the particle position $\vec{r}$. Consequently, whereas the vorticity of the solid body rotation mode is $\vec{\omega} = 2\vec{\Omega}$, the vorticity of the free vortex mode is identically $\vec{\omega} = \vec{0}$.

The sensor we present in this paper correlates the scattered-light burst generated from the pathline of a scattering particle traveling through the probe beam. If this pathline is curved, the sensor cannot distinguish if the curvature is due to solid body rotation or free vortex flow.

Just as curved pathlines do not necessarily imply nonzero vorticity, nonzero vorticity does not necessarily imply that the pathlines are curved. For example, shear flows like one with a velocity

Optics EXPRESS

profile given by $\vec{U} = [\beta x_2, 0, 0]$ where the velocity in the $\hat{x}_1$ direction depends linearly on the $\hat{x}_2$ position scaled with a constant β have straight pathlines in the $\hat{x}_1$ direction but nonzero vorticity: $\vec{\omega} = [0, 0, -\beta]$.

In fluid mechanics, vorticity is commonly interpreted as twice the local angular velocity [35]. We caution the reader that, in general, the angular velocities measured by the sensor we present here *cannot* be interpreted as local angular velocities from which vorticity fields can be deduced but are rather the angular velocities of the tracer particles about their orbit centers. Therefore, these measurements of angular velocity should not be used to calculate vorticity. However, we note that there does exist a special case in which vorticity *can* be deduced from these measurements: when the system is known to be rotating exclusively according to the solid body rotation mode (as in the experiments of Ref. [15]).

Funding. University of Colorado Boulder (Seed Grant Program); National Defense Science and Engineering Graduate Fellowship Program; Air Force Office of Scientific Research (FA9550-17-1-0224); National Science Foundation (Career Award 1554704, DGE 1650115, NSF DMS-1715477).

Acknowledgments. We thank Emily Hannah and Eugene Kwan for helpful discussions.

Disclosures. The authors declare no conflicts of interest.

References

1. B. McKeon, G. Comte-Bellot, J. Foss, J. Westerweel, F. Scarano, C. Tropea, J. Meyers, J. Lee, A. Cavone, R. Schodl, M. Koochesfahani, Y. Andreopoulos, W. Dahm, J. Mullin, J. Wallace, P. Vukoslavčević, S. Morris, E. Pardyjak, and A. Cuerva, "Velocity, vorticity, and mach number," in *Springer Handbooks*, (Springer, 2007), pp. 215–471.
2. Y. Aizu and T. Asakura, *Spatial filtering velocimetry: Fundamentals and applications*, vol. 116 (Springer Science & Business Media, 2006).
3. M. Gaster, "A new technique for the measurement of low fluid velocities," J. Fluid Mech. **20**(2), 183–192 (1964).
4. A. Hayashi and Y. Kitagawa, "Image velocity sensing using an optical fiber array," Appl. Opt. **21**(8), 1394–1399 (1982).
5. M. A. R. Koehl and T. Cooper, "Swimming in an unsteady world," Integr. Comp. Biol. **55**(4), 683–697 (2015).
6. S. Asher and U. Shavit, "The effect of water depth and internal geometry on the turbulent flow inside a coral reef," J. Geophys. Res.: Oceans **124**(6), 3508–3522 (2019). ISBN: 2169-9275 Publisher: Wiley Online Library.
7. E. Bou, A. Ly, J. Roul, O. Llopis, C. Vieu, and A. Cerf, "Compact system for in situ laser Doppler velocimetry of blood flow," Biomed. Opt. Express **10**(11), 5862–5876 (2019).
8. E. P. Hassel and S. Linow, "Laser diagnostics for studies of turbulent combustion," Meas. Sci. Technol. **11**(2), R37–R57 (2000).
9. C. Fang and L. I. U. Hong, "Particle image velocimetry for combustion measurements: Applications and developments," Chin. J. Aeronaut. **31**(7), 1407–1427 (2018).
10. C. Rosales-Guzmán, N. Hermosa, A. Belmonte, and J. P. Torres, "Experimental detection of transverse particle movement with structured light," Sci. Rep. **3**(1), 2815 (2013).
11. F. Durst, J. H. Whitelaw, and A. Melling, *Principles and practice of laser-Doppler anemometry*, Book, Whole (Academic Press, London;New York;, 1981), 2nd ed.
12. A. A. Naqwi and W. C. Reynolds, "Measurement of turbulent wall velocity gradients using cylindrical waves of laser light," Exp. Fluids **10**(5), 257–266 (1991).
13. A. A. Naqwi and S. Petrik, "Fiber-optic dual-cylindrical wave sensor for measurement of wall velocity gradient in a fluid flow," Appl. Opt. **32**(30), 6128–6131 (1993).
14. D. W. Wilson, J. A. Scaif, S. Forouhar, R. E. Muller, F. Taugwalder, M. Gharib, D. Fourguette, and D. Modarress, "Diffractive optic fluid shear stress sensor," in *Diffractive Optics and Micro-Optics*, (Optical Society of America, 2000), p. DThB5.
15. A. Ryabtsev, S. Pouya, A. Safaripour, M. Koochesfahani, and M. Dantus, "Fluid flow vorticity measurement using laser beams with orbital angular momentum," Opt. Express **24**(11), 11762–11767 (2016).
16. M. P. J. Lavery, F. C. Speirits, S. M. Barnett, and M. J. Padgett, "Detection of a Spinning Object Using Light Orbital Angular Momentum," Science **341**(6145), 537–540 (2013).
17. D. Phillips, M. Lee, F. Speirits, S. Barnett, S. Simpson, M. Lavery, M. Padgett, and G. Gibson, "Rotational doppler velocimetry to probe the angular velocity of spinning microparticles," Phys. Rev. A **90**(1), 011801 (2014).
18. M. B. Frish and W. W. Webb, "Direct measurement of vorticity by optical probe," J. Fluid Mech. **107**(-1), 173–200 (1981).
19. A. Belmonte, C. Rosales-Guzmán, and J. P. Torres, "Measurement of flow vorticity with helical beams of light," Optica **2**(11), 1002–1005 (2015).
20. A. J. Majda, A. L. Bertozzi, and A. Ogawa, "Vorticity and incompressible flow. cambridge texts in applied mathematics," Appl. Mech. Rev. **55**(4), B77–B78 (2002).

Optics EXPRESS

21. M. J. Padgett, F. M. Miatto, M. P. J. Lavery, A. Zeilinger, and R. W. Boyd, "Divergence of an orbital-angular-momentum-carrying beam upon propagation," New J. Phys. **17**(2), 023011 (2015).
22. Y. Yeh and H. Cummins, "Localized fluid flow measurements with an he–ne laser spectrometer," Appl. Phys. Lett. **4**(10), 176–178 (1964).
23. L. Drain, "Coherent and noncoherent methods in doppler optical beat velocity measurement," J. Phys. D: Appl. Phys. **5**(3), 481–495 (1972).
24. A. Q. Anderson, E. F. Strong, B. M. Heffernan, M. E. Siemens, G. B. Rieker, and J. T. Gopinath, "Detection technique effect on rotational doppler measurements," Opt. Lett. **45**(9), 2636–2639 (2020).
25. E. F. Strong, "slvel," https://github.com/Liz-Strong/slvel/ (2021).
26. V. Arrizón, U. Ruiz, R. Carrada, and L. A. González, "Pixelated phase computer holograms for the accurate encoding of scalar complex fields," J. Opt. Soc. Am. A **24**(11), 3500–3507 (2007).
27. T. I. Incorporated, "TI DLP LightCrafter 4500 Evaluation Module User's Guide," https://www.ti.com/lit/ug/dlpu011f/dlpu011f.pdf?ts=1595607157534&ref_url=https%253A%252F%252Fwww.ti.com%252Ftool%252FDLPLCR4500EVM (2017).
28. F. Chollet, *et al.*, "Keras," https://github.com/fchollet/keras (2015).
29. M. Abadi, A. Agarwal, P. Barham, E. Brevdo, Z. Chen, C. Citro, G. S. Corrado, A. Davis, J. Dean, M. Devin, S. Ghemawat, I. Goodfellow, A. Harp, G. Irving, M. Isard, Y. Jia, R. Jozefowicz, L. Kaiser, M. Kudlur, J. Levenberg, D. Mané, R. Monga, S. Moore, D. Murray, C. Olah, M. Schuster, J. Shlens, B. Steiner, I. Sutskever, K. Talwar, P. Tucker, V. Vanhoucke, V. Vasudevan, F. Viégas, O. Vinyals, P. Warden, M. Wattenberg, M. Wicke, Y. Yu, and X. Zheng, "TensorFlow: Large-scale machine learning on heterogeneous systems," (2015). Software available from tensorflow.org.
30. L. Fang, Z. Wan, A. Forbes, and J. Wang, "A vectorial doppler effect with spatially variant polarized light fields," (2019).
31. M. Krenn, N. Tischler, and A. Zeilinger, "On small beams with large topological charge," New J. Phys. **18**(3), 033012 (2016).
32. C. Rosales-Guzmán, N. Hermosa, A. Belmonte, and J. P. Torres, "Measuring the translational and rotational velocities of particles in helical motion using structured light," Opt. Express **22**(13), 16504–16509 (2014).
33. Y. Zhai, S. Fu, C. Yin, H. Zhou, and C. Gao, "Detection of angular acceleration based on optical rotational doppler effect," Opt. Express **27**(11), 15518–15527 (2019).
34. E. J. Candès and M. B. Wakin, "An introduction to compressive sampling," IEEE Signal Process. Mag. **25**(2), 21–30 (2008).
35. P. K. Kundu, I. M. Cohen, and D. R. Dowling, *Fluid Mechanics*, 5th edition (Academic Press, 2011).